Journal of Thermal Analysis and Calorimetry (2021) 143:1973–1984
https://doi.org/10.1007/s10973-020-09669-w

Magnetohydrodynamic nonlinear thermal convection nanofluid flow over a radiated porous rotating disk with internal heating

S. Mamatha Upadhya[1] · R. L. V. Renuka Devi[2] · C. S. K. Raju[3] · Hafiz Muhammad Ali[4]

Received: 18 January 2020 / Accepted: 6 April 2020 / Published online: 21 April 2020
© Akadémiai Kiadó, Budapest, Hungary 2020

Abstract

Nonlinear convective flow and heat transfer characteristics are analyzed between stationary nonporous and porous rotating disks utilizing graphene nanoparticles in a water and ethylene glycol base fluid. Heat transfer characteristics are analyzed via incorporating thermal radiation and heat absorption/generation. The governing fluid equations are computed numerically using Runge–Kutta based shooting technique after employing appropriate transformations. Characteristics of sundry variables are elaborated graphically as well as through the construction of Table for water base and ethylene glycol based graphene nanoparticles. It is observed that improvements in nonlinear convection variable owing to temperature and heat generation variable improve wall friction in radial direction. Improvement in Hartman number decreased wall friction in radial and tangential directions along with Nusselt number in graphene/ethylene glycol and graphene/water nanofluid. Ethylene glycol based graphene nanofluid takes less time for execution as compared to water based nanofluid.

Keywords Nanofluid · Nonlinear thermal convection · Heat absorption · Thermal radiation · Nonporous disk Impermeability

Nomenclature

u, v, w	Velocity components of fluid phase in r, ϕ, z directions $\left(\mathrm{ms}^{-1}\right)$
T	Temperature of the nanofluid (K)
T_1	Temperature at fixed impermeable disk (K)
T_2	Temperature at rotating porous disk (K)
υ	Kinematic viscosity $\left(\mathrm{m}^2\,\mathrm{s}^{-1}\right)$
g	Acceleration due to gravity $\left(\mathrm{m\,s}^{-2}\right)$
ρ_{nf}	Density of the nanofluid $\left(\mathrm{kg\,m}^{-3}\right)$
ρ_{f}	Density of the base fluid $\left(\mathrm{kg\,m}^{-3}\right)$
ρ_{s}	Density of the nanoparticles $\left(\mathrm{kg\,m}^{-3}\right)$
μ_f	Dynamic viscosity of the base fluid $\left(\mathrm{kg\ ms}^{-1}\right)$
μ_{nf}	Dynamic viscosity of the nanofluid $\left(\mathrm{kg\ ms}^{-1}\right)$
c_{pf}	Specific heat capacity at constant pressure of the fluid $(\mathrm{J\,kg}^{-1}\mathrm{K}^{-1})$
k_{nf}	Thermal conductivity $(\mathrm{W\,m}^{-1}\mathrm{K}^{-1})$
$\left(\rho c_{\mathrm{p}}\right)_{\mathrm{nf}}$	Effective heat capacity $\left(\mathrm{kg\,m}^{-3}\mathrm{K}^{-1}\right)$
$(\rho c_{\mathrm{p}})_{\mathrm{p}}$	Effective heat capacity of the particle medium $(\mathrm{kg\,m}^{-3}\mathrm{K}^{-1})$
α_{nf}	Diffusion coefficient $(\mathrm{m}^2\mathrm{s}^{-1})$
v_{nf}	Kinematic viscosity $(\mathrm{m}^2\mathrm{s}^{-1})$
σ^*	Stefan–Boltzmann constant $(\mathrm{W\ m\,K}^{-4})$
σ	Electrical conductivity $\left(\mathrm{S\,m}^{-1}\right)$
k^*	Mean absorption coefficient
M	Hartman Number
ϕ	Nano particle volume fraction
Pr	Prandtl number
R	Radiation parameter
Q	Heat generation/absorption coefficient
ζ	Similarity variable
C_{f}	Skin friction coefficient
Nu_{x}	Local Nusselt number
Re	Local Reynolds number
l	Distance between two disks
Ω	Angular speed of the rotating disk

✉ Hafiz Muhammad Ali
hafiz.ali@kfupm.edu.sa

S. Mamatha Upadhya
mamathasupadhya@gmail.com

C. S. K. Raju
sivaphd90@gmail.com

1 Department of Mathematics, Kristu Jayanti College, Autonomous, Bangalore, Karnataka 560077, India

2 Department of Mathematics, Sri Venkateswara University, Tirupati 517502, India

3 Department of Mathematics, GITAM School of Science, GITAM University, Bangalore, Karnataka, India

4 Mechancal Engineering Department, King Fahd University of Petroleum and Minerals, Dhahran 31261, Saudi Arabia

ε	Measure of the angular speed or momentum of the of the rotating porous disk
W	Suction velocity at which fluid is withdrawn from the rotating porous disk (Injection if W is negative.)
α_1	Thermal buoyancy variable
β_t	Nonlinear convection variable
δ	Heat generation variable

Introduction

In recent years, the problem of fluid flow flanked by the rotating surfaces has drawn substantial attention of the researchers owing to its numerous applications in engineering and industrial fields; for example, in rotating machinery, thermal-power system, aeronautical systems, medical equipment, gas turbine rotors, storage devices in computers, air cleaning machines, crystal growth process and food-processing technology. Wu et al. [1] took up experimental investigation of the flow over grooved rotating disk. Rizwan et al. [2] simulated numerically magnetite nanoparticles considering water as base fluid between two parallel disks. Turkyilmazoglu [3–5] investigated fluid flow over rotating moving disk. Rashidi et al. [6, 7] reported MHD nanofluid flow considering porous rotating disk. Qayyum et al. [8] took up comparative scrutiny of fluid flow over a rotating disk by considering five nanoparticles. Pourmehran et al. [9] reported rheological characteristic of metal-based nanofluid flow between rotating disks. Attia [10] studied steady flow considering porous medium on a rotating disk. Mellor et al. [11] investigated flow amid rotating and stationary disks. Kavenuke et al. [12] modeled flow amid porous rotating disk and a fixed impermeable disk. Awati et al. [13] studied the flow amid porous rotating and fixed impermeable disk.

Constant advancement in the electronic equipment frequently faces the challenges pertaining to the thermal management from declining accessible to surface area for heat exclusion or from the improved phase of heat generation. These challenges could be conquered with modeling the cooling equipment with optimal geometry or by increasing heat transfer characteristics. Choi [14] suggested that nanofluid in this context will sort out all these issues. Sarafraz et al. [15] studied convective boiling heat transfer of CuO-water/ethylene glycol nanofluid. Salari et al. [16] studied thermal behavior of aqueous iron oxide nanofluid on a flat disk. Kamalgharibi et al. [17] took up experimental study on the stability of CuO nanoparticles dispersed in different base fluids. Sajid et al. [18] studied thermal conductivity of hybrid nanofluid. Imtiaz et al. [19] demonstrated convective flow between rotating stretchable disks considering carbon nanotubes and thermal radiation effects. Salari et al. [20] studied boiling thermal performance of TiO_2 aqueous nanofluid on a disk copper block. Hayat et al. [21] reported induced magnetic field and melting heat transfer effects along with variable thickness on nanofluid flow along a rotating disk. Bachok et al. [22] portrayed flow and heat transport of nanofluid on a porous revolving disk. Ellahi et al. [23] carried out simulation of spherically shaped hydrogen bubbles with stenosis through a tube nozzle. Ellahi et al. [24] probed the impact of hybrid nanofluid flow with the slip effects. Nazari et al. [25] investigated mixed convective non-Newtonian nanofluid in a lid-driven square cavity. Maleki et al. [26, 27] investigated flow and heat transfer in nanofluid considering various parameters. Giwa et al. [28] addressed heat, flow and mass transfer considering hybrid nanofluid. Peng [29] investigated energy performance along a U-shaped evacuated solar tube via considering oxide nanoparticles. Ahmadi [30] took up machine learning approach to study dynamic viscosity of nanofluid. Yousefzadeh et al. [31] studied convection in nanofluid in a cavity. Arasteh et al. [32] explored heat and fluid flow of nanofluid in a double-layered sinusoidal heat sink. Sarafraz et al. [33] investigated on thermal analysis and thermo-hydraulic characteristics of zirconia-water nanofluid. Maleki et al. [34] addressed flow and heat transfer of pseudo-plastic nanofluid with viscous dissipation over a moving permeable plate. Thus, researchers [35–44] have observed anomalously that diffusion of nanometer-sized solid particles in the base fluid shows high effective thermal conductivity, longer suspension time, larger surface area, lower clogging and erosion, significant energy saving and lower operating cost. Thermal conductivity of nanofluid is enhanced with suspension of metallic or non-metallic particles. Hence, carbon materials such as graphite nanoparticles, carbon nanotubes, exfoliated graphite, diamond nanoparticles, nanofibers, carbon black and graphene have gained more importance due to low density and large intrinsic thermal conductivity compared to metal/metal oxides.

Recent studies reveal that graphene, a perfect two-dimensional lattice of carbon, has a very high thermal conductivity with many unique chemical, physical and mechanical properties. Hence, graphene material has emerged as a fascinating material of the carbon in the field of technology and science. Graphene can be offered in granular form, and hence it could be dispersed in organic solvents, water and polymers which are advantageous in super conductors, lithium ion batteries, gas censors, fabrication of transparent conductive films, solar cells, advanced electronics, etc. Keeping this into view, the authors [45–49] studied flow, heat and mass transfer with the inclusion of graphene nanoparticles on various flow configurations.

Constantly engineers and researchers are looking forward to scrutinize the fluids subjected to the thermal radiation as it has major influence in high-temperature processes, for instance, in nuclear power plants, gas turbines, satellites, power generation, combustion and polymer processing industry. Mamatha et al. [50–53] portrayed non-Newtonian flow and heat transform over different geometry considering deferment of dust particles and nanoparticles. Sharma et al. [54] investigated buoyancy effects on unsteady convection radiating fluid over a vertically moving porous plate. Santhosh et al. [55] studied radiated convective Carreau nanofluid flow with heat generation. Nayak et al. [56] investigated viscous dissipation and partial slip influence on the radiative nano-Tangent hyperbolic fluid over permeable Riga plate. Eid and Makinde [57] studied effects of solar radiation on a MHD nanofluid flow over a porous medium considering chemically reactive species.

The aim of the current theoretical model is to investigate the nonlinear convective flow between the stationary nonporous and porous rotating disks utilizing graphene nanoparticles in a water and ethylene glycol base fluid. Heat transfer distinctiveness is analyzed considering thermal radiation and heat absorption/generation. The governing fluid equations are computed using Runge–Kutta based shooting method. Characteristics of sundry variables are elaborated graphically and through the construction of Table.

Mathematical formulation

Steady nonlinear nanofluid flow (water and graphene, ethylene glycol and graphene) between the stationary and porous disks is considered in this study. Nanofluid motion is generated by the rotary motion of porous disk as well as suction/injection of nanofluid. Rotating and stationary disks are separated by the distance l. Compared to the radii of the disk, the distance l is very small. Transverse magnetic field with strength B_0 acts all along the z direction. The process of heat transfer occurs due to heat absorption/generation and thermal radiation. Path of fluid flow is indicated with arrows (see Fig. 1) heading towards the porous disk which is rotating with constant angular speed Ω about the z axis with the rotation speed $\Omega\varepsilon$, and ε is a regulator which controls rotation of the disk. When $\varepsilon = 0$ no rotation takes place and $\varepsilon > 0$ rotation exists and $(0 \leq \varepsilon \leq 1)$. Here, the suction velocity W is assumed to be constant.

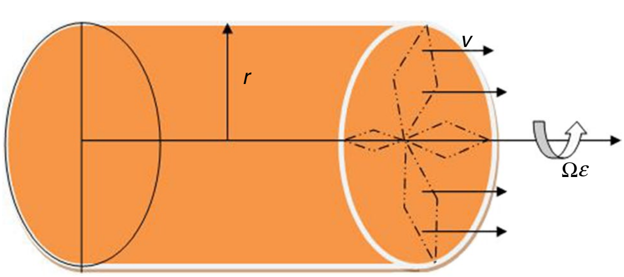

Fig. 1 Geometry of flow model

Considering the above said assumptions and following (Hayat et al. [17, 21] and Kavenuke et al. [12], the flow model is governed by the subsequent equations.

$$\left(\frac{1}{r}\right)\frac{\partial}{\partial r}(ru) + \frac{\partial w}{\partial z} = 0 \tag{1}$$

$$u\frac{\partial u}{\partial r} + w\frac{\partial u}{\partial z} - \left(\frac{v^2}{r}\right) + \frac{1}{\rho_{\mathrm{nf}}}\frac{\partial p}{\partial r} = \left(\begin{array}{l} \upsilon_{\mathrm{nf}}\left[\frac{\partial^2 u}{\partial r^2} + \frac{\partial}{\partial r}\left(\frac{u}{r}\right) + \frac{\partial^2 u}{\partial z^2}\right] - \frac{\sigma_{\mathrm{f}} B_0^2 u}{\rho_{\mathrm{f}}} + \\ \left(\left(\frac{1}{\rho_{\mathrm{f}}}\right) g\left[(\rho\beta)_{\mathrm{nf}}(T - T_2) + (\rho\beta_1)_{\mathrm{nf}}(T - T_2)^2\right]\right) \end{array}\right) \tag{2}$$

$$\frac{u}{r}\frac{\partial}{\partial r}(rv) + w\frac{\partial v}{\partial z} = \upsilon_{\mathrm{nf}}\left[\frac{\partial^2 v}{\partial r^2} + \frac{\partial}{\partial r}\left(\frac{v}{r}\right) + \frac{\partial^2 v}{\partial z^2}\right] - \frac{\sigma_{\mathrm{f}} B_0^2 v}{\rho_{\mathrm{f}}} \tag{3}$$

$$u\frac{\partial w}{\partial r} + w\frac{\partial w}{\partial z} + \left(\frac{1}{\rho_{\mathrm{nf}}}\right)\frac{\partial p}{\partial z} = \left(\upsilon_{\mathrm{nf}}\right)\left[\left(\frac{1}{r}\right)\frac{\partial w}{\partial r} + \frac{\partial^2 w}{\partial r^2} + \frac{\partial^2 w}{\partial z^2}\right] \tag{4}$$

$$\begin{aligned} u\frac{\partial T}{\partial r} + w\frac{\partial T}{\partial z} = \alpha_{\mathrm{nf}}\left[\left(\frac{1}{r}\right)\frac{\partial T}{\partial r} + \frac{\partial^2 T}{\partial r^2} + \frac{\partial^2 T}{\partial z^2}\right] \\ + \frac{Q}{(\rho c_{\mathrm{p}})_{\mathrm{nf}}}(T - T_2) + \frac{16}{3}\frac{\sigma^*}{k^*}\frac{T_2^3}{(\rho c_{\mathrm{p}})_{\mathrm{nf}}} \\ \left[\frac{\partial^2 T}{\partial r^2} + \frac{1}{r}\frac{\partial T}{\partial r} + \frac{\partial^2 T}{\partial z^2}\right]. \end{aligned} \tag{5}$$

Boundary conditions (following Kavenuke et al. [12]) are given by

- With reference to fixed impermeable disk at$z = 0$

$$\begin{aligned} &u(r,0) = 0 \\ &v(r,0) = 0 \\ &w(r,0) = 0 \\ &T(r,0) = T_1 \end{aligned} \tag{6}$$

- With reference to porous disk at$z = l$

$$\begin{aligned} & u(r,l) = 0 \\ & v(r,l) = r\Omega \\ & w(r,l) = \varepsilon W \\ & T(r,l) = T_2 \end{aligned}. \tag{7}$$

Here, (u, v, w) specify the velocity components along the (r, ϕ, z) directions, T the temperature of the nanofluid, T_1 the temperature at fixed impermeable disk, T_2 the temperature at rotating porous disk, υ_{nf} represents the nanofluid kinematic viscosity, p the pressure and ρ_{nf} the density of the nanofluid, α_{nf} and $(\rho c_p)_{nf}$ signify the thermal diffusivity and effective heat capacity of nanofluid, Q the heat (generation, absorption), and Stefan–Boltzmann constant and coefficient of mean absorption are represented as σ^* and k^*.

Following Bachok et al. [22]

$$\left.\begin{array}{l} \rho_{nf} = \phi\rho_s + (1-\phi)\rho_f,\ \mu_{nf} = \mu_f(1-\phi)^{-2.5},\ \left(\rho c_p\right)_{nf} = \phi\left(\rho c_p\right)_s + (1-\phi)\left(\rho c_p\right)_f, \\ \frac{k_{nf}}{k_f} = \frac{-\phi(n-1)\left(k_f-k_s\right)+k_s+(n-1)k_f}{k_s+(n-1)k_f+\phi\left(k_f-k_s\right)},\ (\rho\beta)_{nf} = (1-\phi)(\rho\beta)_f + \phi(\rho\beta)_s, \end{array}\right\}. \tag{8}$$

Here, ϕ represents the solid volume fraction of the nanoparticles, (μ_{nf}, μ_f) indicate the nanofluid effective and base fluid dynamic viscosity, $(\rho_{nf}, \rho_f, \rho_s)$ signify the density of nanofluid, base fluid and density of the solid nanoparticles and (k_{nf}, k_f) the thermal conductivity of nanofluid and base fluid, and $(\rho\beta)_{nf}$ is volumetric thermal expansion coefficient.

We considered the following transformations following Awati et al. [13] and Mellor et al. [11]:

Velocity components in terms of stream function are considered as

$$u = \frac{1}{r}\frac{\partial\psi}{\partial z},\quad w = -\frac{1}{r}\frac{\partial\psi}{\partial r}. \tag{9}$$

Similarity variable and physical stream function are

$$\zeta = \frac{z}{l} = \frac{\Omega z}{W} \quad \text{and} \quad \psi(r,n) = r^2 f(\zeta)W. \tag{10}$$

Thus, from (9) and (10) radial and axial velocity components are

$$\frac{u}{r} = \Omega\left(f'(\zeta)\right),\quad \frac{w}{W} = -2(f(\zeta)). \tag{11}$$

Tangential velocity and pressure variable are

$$v = r\Omega g(\zeta),\quad p = \frac{1}{2}\rho r^2\Omega^2 A + \rho W^2 P(\zeta). \tag{12}$$

Non-dimensional temperature is given by

$$\theta(\zeta) = \frac{T-T_2}{T_1-T_2}. \tag{13}$$

Applying the transformation from Eqs. (11), (12) and (13) in Eqs. (1)–(7) and (8), one obtains

$$\left[\left(\frac{1}{\mathrm{Re}}\right)\left(\frac{1}{(1-\phi)^{2.5}\left((1-\phi)+\phi\frac{\rho_s}{\rho_f}\right)}\right)\right]\frac{d^3f}{d\zeta^3} = \left(\begin{array}{l} \left[\begin{array}{l} \left(\frac{df}{d\zeta}\right)^2 - 2f(\zeta)\frac{d^2f}{d\zeta^2} \\ -g^2(\zeta) - A \end{array}\right] + (M)\frac{df}{d\zeta} \\ -\theta(\zeta)\alpha_1\left[\begin{array}{l} \left((1-\phi)+\left(\frac{\phi(\rho\beta)_s}{(\rho\beta)_f}\right)\right)+ \\ \beta_t\theta(\zeta)\left((1-\phi)+\left(\frac{\phi(\rho\beta)_s}{(\rho\beta)_f}\right)\right) \end{array}\right] \end{array}\right) \tag{14}$$

$$\left[\left(\frac{1}{\mathrm{Re}}\right)\left(\frac{1}{(1-\phi)^{2.5}\left((1-\phi)+\phi\frac{\rho_s}{\rho_f}\right)}\right)\right]\frac{d^2g}{d\zeta^2} = \left[2\frac{df}{d\zeta}g(\zeta) - 2f(\zeta)\frac{dg}{d\zeta} + Mg(\zeta)\right] \tag{15}$$

$$\left[\left(\frac{2}{\mathrm{Re}}\right)\left(\frac{1}{(1-\phi)^{2.5}\left((1-\phi)+\phi\frac{\rho_s}{\rho_f}\right)}\right)\right]\frac{\mathrm{d}^2f}{\mathrm{d}\zeta^2}=\left[-P'(\zeta)-4f(\zeta)\frac{\mathrm{d}f}{\mathrm{d}\zeta}\right] \tag{16}$$

$$\left[\frac{k_{nf}}{k_f\left((1-\phi)+\frac{(\rho c_p)_s}{(\rho c_p)_f}\phi\right)}+\frac{4}{3}R\right]\frac{\mathrm{d}^2\theta}{\mathrm{d}\zeta^2}=(\mathrm{Pr})(\mathrm{Re})\left[\left(2f(\zeta)\frac{\mathrm{d}\theta}{\mathrm{d}\zeta}\right)-\frac{\delta\theta(\zeta)}{\left((1-\phi)+\frac{(\rho c_p)_s}{(\rho c_p)_f}\phi\right)}\right] \tag{17}$$

$$f(0)=0,\ \theta(0)=1,\ g(0)=0,\ f'(0)=0$$

$$\theta(1)=0, f'(1)=0,\ g(1)=1, f(1)=-\left(\frac{\varepsilon}{2}\right). \tag{18}$$

Here, $\mathrm{Re}=\frac{W^2}{\Omega v_f}$ signifies Reynolds number,$M=\frac{\sigma B_0^2}{\Omega \rho_f}$ Hartman number, $\alpha_1=\frac{g\beta_f(T_1-T_2)}{r\Omega^2}$ thermal buoyancy (or mixed convection) variable, A is the arbitrary constant,$\beta_t=\frac{\beta_{1f}(T_1-T_2)}{\beta_f}$ nonlinear convection variable owing to temperature, $\delta=\frac{Q}{\Omega(\rho c_p)_f}$ heat generation variable, $\mathrm{Pr}=\frac{(\mu c_p)_f}{k_f}$ Prandtl number, and $R=\frac{16\sigma^* T_2^3}{3k^* k_f}$ is the radiation parameter.

Expression of coefficient of skin friction (radial and tangential direction) and Nusselt number: Following Imtiaz et al. [19]

$$C_{fr}(R_e)^{\frac{1}{2}}=\frac{1}{(1-\phi)^{2.5}}\frac{\mathrm{d}^2f(0)}{\mathrm{d}\zeta^2},\quad C_{f\phi}(R_e)^{\frac{1}{2}}=\frac{1}{(1-\phi)^{2.5}}\frac{\mathrm{d}g(0)}{\mathrm{d}\zeta},$$

$$Nu(R_e)^{-\frac{1}{2}}=-\frac{k_{nf}}{k_f}\left(1+\frac{4}{3}R\right)\frac{\mathrm{d}\theta(0)}{\mathrm{d}\zeta}. \tag{19}$$

Method of Numerical solution

The nonlinear differential conditions (14)–(17) subject to conditions (18) originate from the third solicitation in f and the second solicitation in g and θ. These conditions can be seen numerically utilizing a fourth solicitation Runge–Kutta technique that consolidates a terminating framework and Newton–Raphson innovation. We portray here ($\xi=\zeta$)

$$\begin{gathered}f=Y_1,\ \frac{\partial f}{\partial\xi}=Y_2,\ \frac{\partial^2 f}{\partial\xi^2}=Y_3,\ g=Y_4,\ \frac{\partial g}{\partial\xi}=Y_5,\ \theta=Y_6,\ \frac{\partial\theta}{\partial\xi}=Y_7\\(1-\phi)^{2.5}\left((1-\phi)+\phi\frac{\rho_s}{\rho_f}\right)=A_1,\left((1-\phi)+\left(\frac{\phi(\rho\beta)_s}{(\rho\beta)_f}\right)\right)=B_1,\left((1-\phi)+\frac{(\rho c_p)_s}{(\rho c_p)_f}\phi\right)=C_1.\end{gathered} \tag{20}$$

We also define the following:

$$f=F_1,\frac{\partial f}{\partial\xi}=F_2,\frac{\partial^2 f}{\partial\xi^2}=F_3, g=F_4,\frac{\partial g}{\partial\xi}=F_5,\frac{\partial\theta}{\partial\xi}=F_7. \tag{21}$$

Substituting conditions (20) and (21) by conditions (18) transformed to an arrangement of nine synchronous conditions of the principal request as follows:

$$F_1=Y_2, \tag{22}$$

$$F_2=Y_3, \tag{23}$$

$$F_3=\left(\left[(F_2)^2-2F_1F_3-F_4^2-A\right]+(M)F_2-F_6\alpha_1\left[B_1+\beta_tF_5\right]\right). \tag{24}$$

In a similar way we have converted other two equations with higher derivatives (F_5', F_7') into initial value problem as mentioned above and the boundary conditions are given as follows:

$$F_1(0)=0,\ \ F_2(0)=0,\ \ Y_4(0)=0,\ \ Y_6(0)=1,\ \ Y_2(1)=1,\ \ Y_4(1)=1,\ \ Y_2(1)=1\ldots\ldots \tag{25}$$

Here, ξ_∞ is selected as $\xi_\infty=1$. The unclear introductory conditions are taken as $Y_3(0)=s,\ Y_5(0)=t$ and $Y_7(0)=p$. We utilize the Newton–Raphson technique to discover $s,\ t$ and q with the goal that the arrangements of the conditions (25) fulfill as far as possible conditions (18). Right now, start with the underlying evaluations ($p(0),\ t(0),\ s(0)$) through

Table 1 Thermophysical features of base fluid (EG), water and nanoparticles (graphene) (Mamatha et al. [53])

Thermophysical properties	Water	Ethylene glycol	Graphene
$\rho/\text{Kg m}^{-3}$	997.1	1115	2250
$k/\text{Wm}^{-1}\text{K}^{-1}$	0.613	0.253	2500
$c_p/\text{JKg}^{-1}\text{K}^{-1}$	4179	2430	2100

the trigger strategy. The Newton–Raphson calculation is stretched out to incorporate the halfway subordinates of the components of every factor. This will create the subordinates of $F(F_1,\ F_2,\ ...,\ F_5)$ on $p,\ t$ and s as follows:

$$F_{\text{p}}(F_6,\ F_7,\ ...\ F_{10}),\quad F_{\text{t}}(F_{11},\ F_{12},\ ...\ F_{15}),\quad F_{\text{s}}(F_{16},\ F_{17},\ ...\ F_{20}). \tag{26}$$

Thus, we need to find $F_{\text{p}} = 0,\ F_{\text{t}} = 0,\ F_{\text{s}} = 0$, simultaneously. Following Cebeci and Keller, these yield a system of algebraic equations which satisfy the boundary conditions when $\xi = 0$.

Table 2 Coefficient of skin friction $\left(c_{\text{f}}/\text{Re}^{\frac{1}{2}}, c_{\text{g}}/\text{Re}^{\frac{1}{2}}\right)$ and Nusselt number $\left(-Nu/\text{Re}^{-\frac{1}{2}}\right)$ for Graphene + H_2O nanofluid

Re	R	M	β_t	δ	$c_{\text{f}}/\text{Re}^{\frac{1}{2}}$	$c_{\text{g}}/\text{Re}^{\frac{1}{2}}$	$\left(-Nu/\text{Re}^{-\frac{1}{2}}\right)$	Elapsed time (s)
0.1					0.046255	0.992487	2.887949	0.713823
0.2					0.083889	0.934527	4.381084	
0.3					0.114505	0.878343	6.166715	
	0.5				0.024728	1.021418	2.290404	0.668670
	1				0.024401	1.021421	3.535253	
	1.5				0.024075	1.021424	4.995193	
		1			0.024657	1.017207	2.290391	0.627631
		5			0.024506	0.984380	2.290288	
		10			0.023461	0.945386	2.290168	
			0.1		0.024085	1.021421	2.290360	0.633488
			0.2		0.024728	1.021418	2.290404	
			0.3		0.025372	1.021415	2.290448	
				0	0.024689	1.021418	2.323660	0.639627
				0.5	0.024892	1.021416	2.154818	
				1	0.025108	1.021414	1.979244	

Table 3 Coefficient of skin friction $\left(c_{\text{f}}/\text{Re}^{\frac{1}{2}}, c_{\text{g}}/\text{Re}^{\frac{1}{2}}\right)$ and Nusselt number $\left(-Nu/\text{Re}^{-\frac{1}{2}}\right)$ for Graphene + EG nanofluid

Re	R	M	β_t	δ	$c_{\text{f}}/\text{Re}^{\frac{1}{2}}$	$c_{\text{g}}/\text{Re}^{\frac{1}{2}}$	$\left(-Nu/\text{Re}^{-\frac{1}{2}}\right)$	Elapsed time (s)
0.1					0.048561	0.992807	7.844818	0.658709
0.2					0.077066	0.935420	15.820617	
0.3					0.101257	0.879769	24.045523	
	0.5				0.029529	1.021543	4.363944	0.499480
	1				0.027491	1.021560	7.995235	
	1.5				0.025768	1.021573	12.894400	
		1			0.029454	1.017352	4.363862	0.477742
		5			0.028873	0.984668	4.363231	
		10			0.028191	0.945836	4.362492	
			0.1		0.028673	1.021546	4.363627	0.459286
			0.2		0.029529	1.021543	4.363944	
			0.3		0.030385	1.021540	4.364212	
				0	0.029354	1.021545	4.477382	0.478427
				0.5	0.030304	1.021537	3.879228	
				1	0.031480	1.021527	3.187584	

Table 4 Comparison of $\frac{\mathrm{d}^2 f(0)}{\mathrm{d}\zeta^2}$ for various values of Ω when $M = \alpha_1 = \delta = \Upsilon_1 = \Upsilon_2 = \phi = 0$, and $\mathrm{Re} = 1$

Ω	Stewartson [58]	Imtiaz et al. [19]	Present results
0.5	0.06663	0.06663	0.0667
0	0.09997	0.09997	0.09998
− 0.8	0.08394	0.08384	0.00848
− 1	0.06666	0.06666	0.06666

Table 5 Comparison of $\left(-\frac{\mathrm{d}g(0)}{\mathrm{d}\zeta}\right)$ for various values of Ω when $M = \alpha_1 = \delta = \Upsilon_1 = \Upsilon_2 = \phi = 0$, and $\mathrm{Re} = 1$

Ω	Stewartson [58]	Imtiaz et al. [19]	Present results
0.5	0.50261	0.50261	0.5026
0	1.00428	1.00428	1.0043
− 0.8	1.80259	1.80259	1.80259
− 1	2.00095	2.00095	2.00096

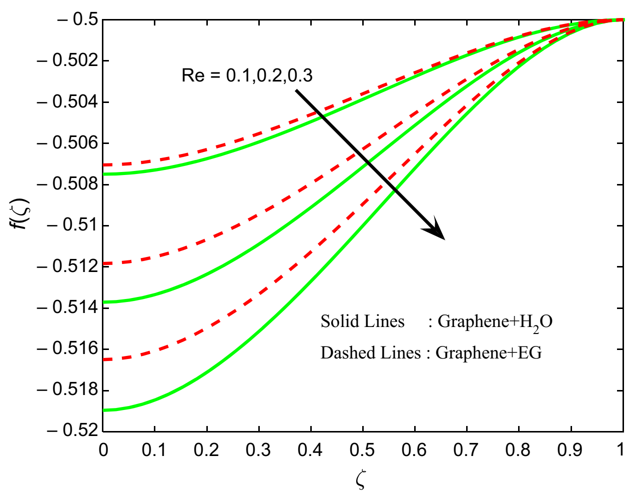

Fig. 2 Behavior of nanofluid axial velocity for various Re

$$f'_\zeta p + f'_t t + f'_s s + f' = 0,\quad g_\zeta p + g_t t + g'_s s + \theta = 0,$$
$$\theta_p p + \theta_t t + \theta'_s s + \theta = 0. \tag{27}$$

Revamping the framework in condition (27) yields a grid condition AX = B:

$$\begin{bmatrix} f'_\zeta & f'_t & f'_s \\ g_\zeta & g_t & g_s \\ \theta_\zeta & \theta_t & \theta_s \end{bmatrix}\begin{bmatrix} p \\ t \\ s \end{bmatrix} = \begin{bmatrix} -f' \\ -g \\ -\theta \end{bmatrix}. \tag{28}$$

This lattice condition can be found by Cramer's standard. The following estimation of p, t and can be computed by using the following formula:

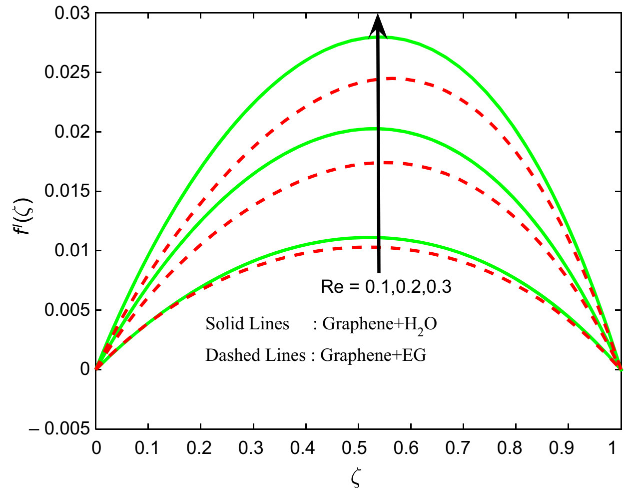

Fig. 3 Behavior of nanofluid radial velocity for various Re

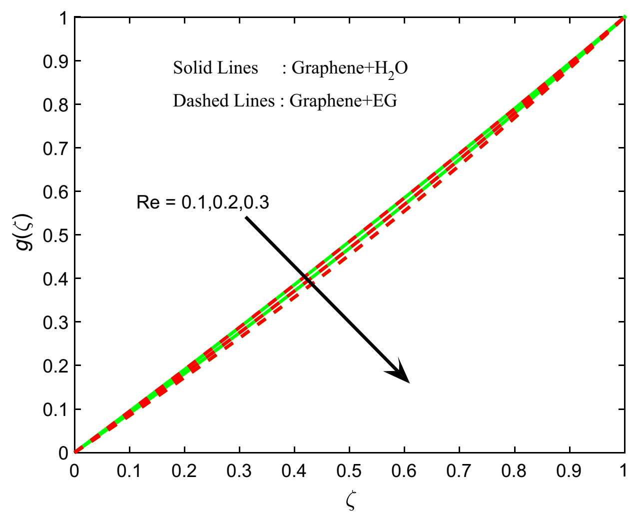

Fig. 4 Behavior of nanofluid tangential velocity for various Re

$$p^{(\mathrm{new})} = p^{(\mathrm{old})} + \frac{\det\left(A_{\mathrm{B}}(I,J)\right)}{\det(A)},$$
$$t^{(\mathrm{new})} = t^{(\mathrm{old})} + \frac{\det\left(A_{\mathrm{B}}(I,J)\right)}{\det(A)},$$
$$s^{(\mathrm{new})} = s^{(\mathrm{old})} + \frac{\det\left(A_{\mathrm{B}}(I,J)\right)}{\det(A)}. \tag{29}$$

When the estimations of p, t and s are known, we utilized the Runge–Kutta strategy to tackle the main request of common differential conditions $F_1, F_2, \ldots, F_{20}$. For arrangement, the most extreme supreme relative difference between two methods is employed inside a pre-doled out resilience $\varepsilon < 10^{-6}$. In the process, the distinction meets the grouping criteria, the arrangement is projected to have amalgamated and the iterative procedure is ended.

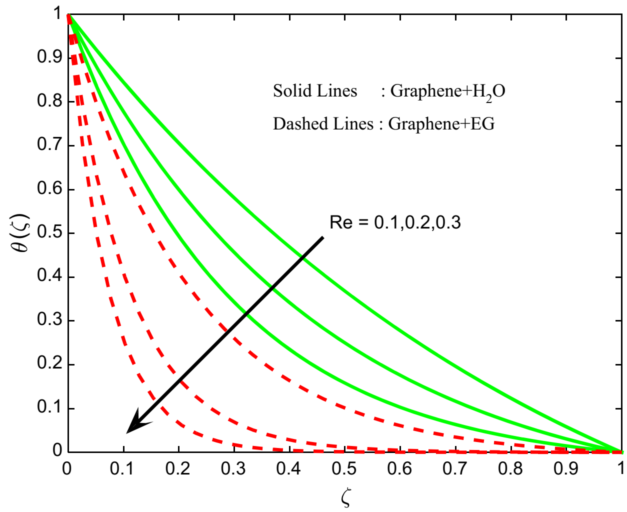

Fig. 5 Behavior of nanofluid temperature for various Re

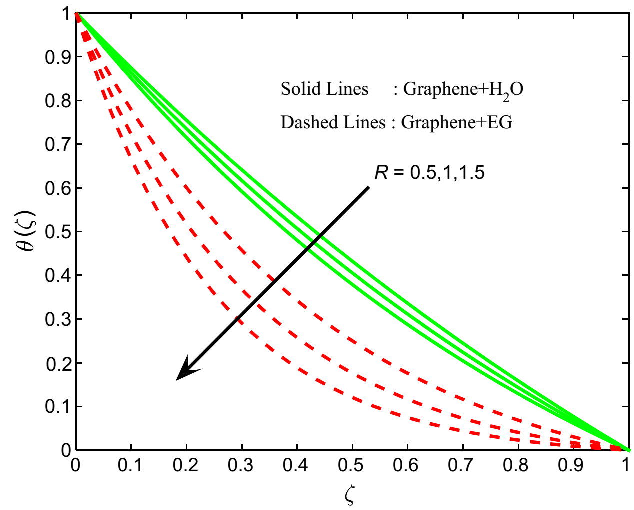

Fig. 7 Behavior of nanofluid temperature for various R

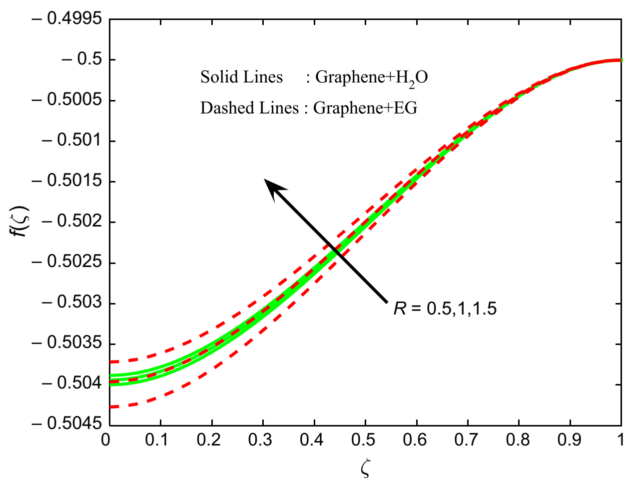

Fig. 6 Behavior of nanofluid axial velocity for various R

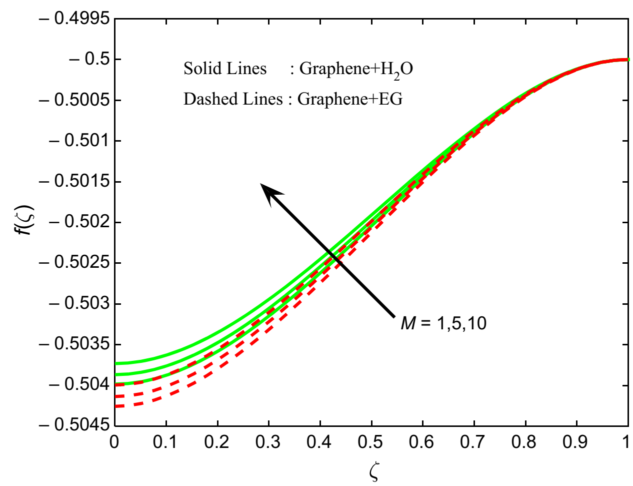

Fig. 8 Behavior of nanofluid axial velocity for various M

Validation of the numerical procedure

To check the numerical program, the outcomes were contrasted with those recently announced in the writing. We thought about the particular qualities of the stream parameters with the investigation consequences of existing writing. These examinations are contrasted in Tables 4 and 5. It is discovered that the examination is satisfactory and reliable with the current outcomes.

Results and discussion

The influence of relevant variables $\mathrm{Re} = 0.051$, $\phi = 0.02$, $R = 0.5$, $\delta = 0.1$, $A = 0.4$, $M = 0.5, \beta_t = 0.2$, $\alpha_1 = 0.2$ on velocities (axial $f(\zeta)$, tangential $g(\zeta)$ and radial $f'(\zeta)$), temperature $\theta(\zeta)$, skin friction $\left(c_f(\mathrm{Re})^{\frac{1}{2}}, c_g(\mathrm{Re})^{\frac{1}{2}}\right)$ and Nusselt number $\left(-Nu(\mathrm{Re})^{-\frac{1}{2}}\right)$ for Graphene $+ H_2O$ and Graphene $+ EG$ nanofluid are discussed in this section. Thermophysical features of water, ethylene glycol and graphene are illustrated in Table 1. The coefficient of skin friction (radial and tangential direction), and Nusselt number for Graphene $+ H_2O$ and Graphene $+ EG$ nanofluid are portrayed in Tables 2 and 3. In Tables 4 and 5, comparison of obtained results with the published results of Stewartson [31] and Imtiaz et al. [19] for various values of Ω is tabulated and excellent agreement is observed with the published results.

Figures 2–5 expose the influence of Reynolds number (Re) on axial $f(\zeta)$, radial $f'(\zeta)$ tangential $g(\zeta)$ velocity and temperature $\theta(\zeta)$. It is observed that intensification in Re ensures decrement in $f(\zeta)$,$g(\zeta)$ and $\theta(\zeta)$, whereas $f'(\zeta)$

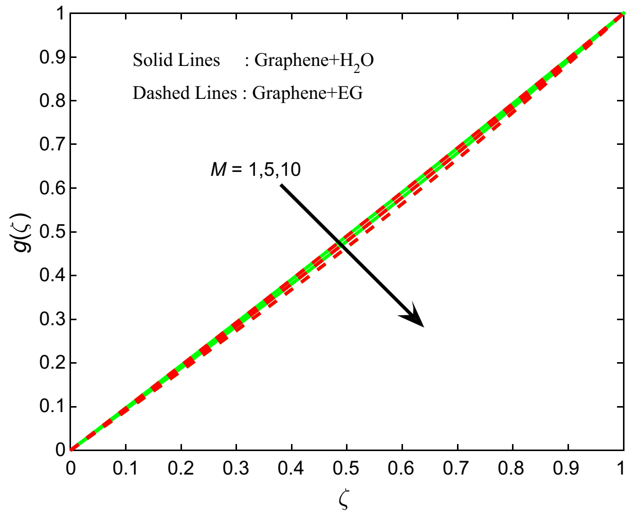

Fig. 9 Behavior of nanofluid tangential velocity for various M

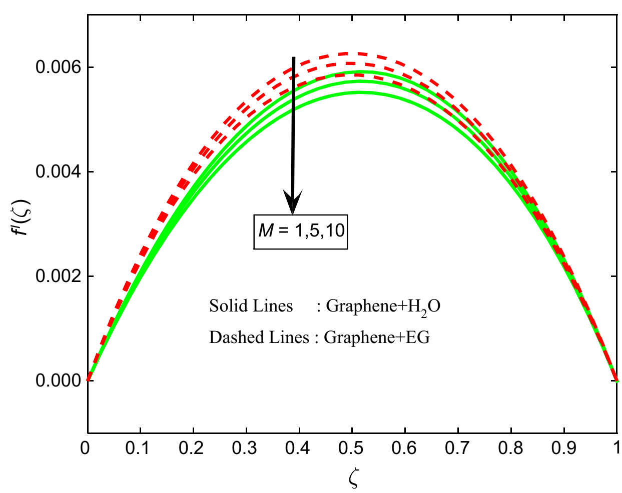

Fig. 10 Behavior of nanofluid radial velocity for various M

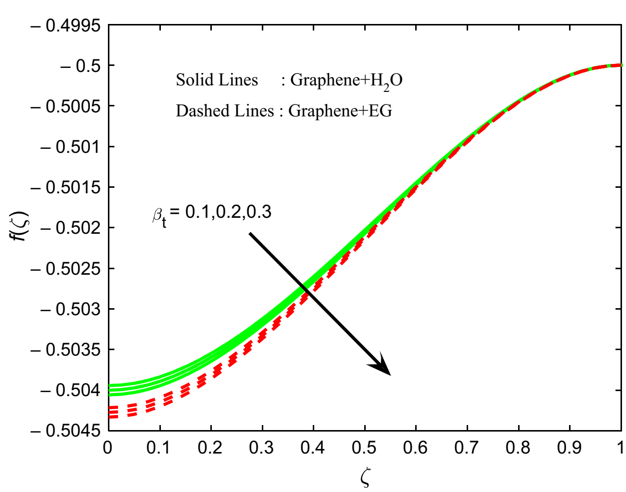

Fig. 11 Behavior of nanofluid axial velocity for various β_t

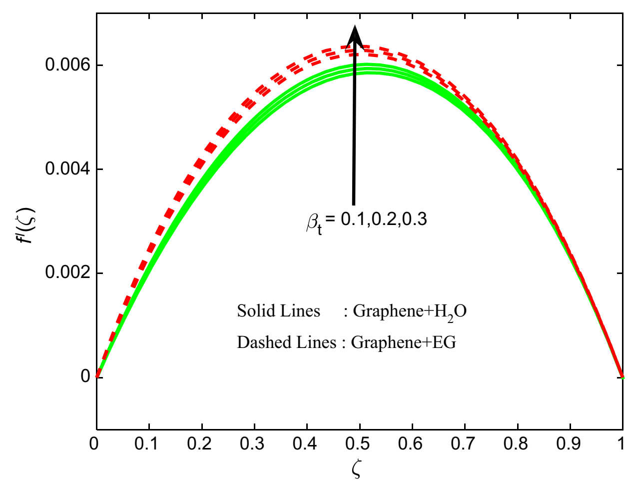

Fig. 12 Behavior of nanofluid radial velocity for various β_t

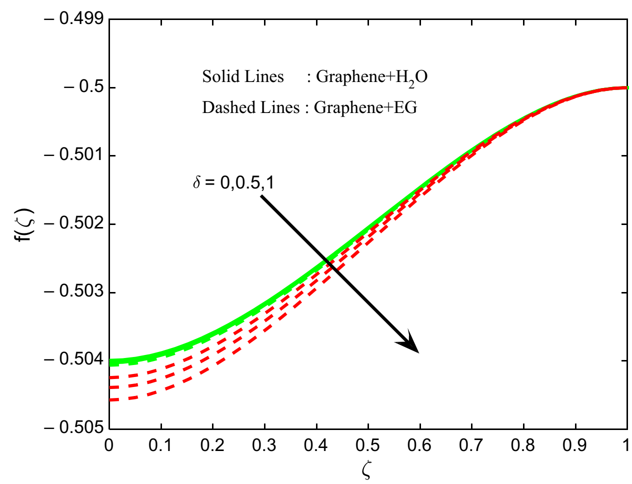

Fig. 13 Behavior of nanofluid axial velocity for various δ

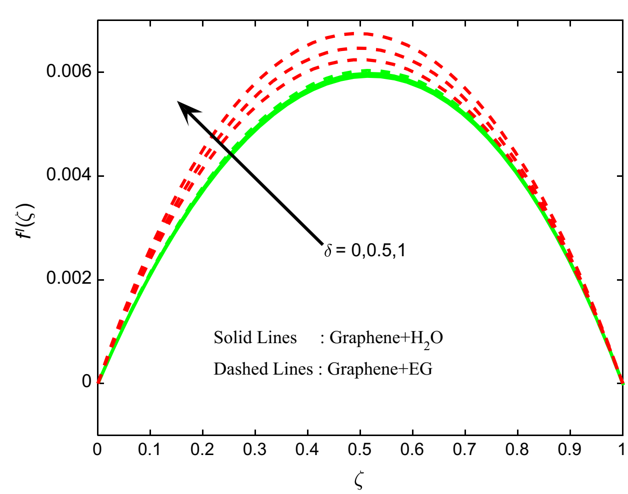

Fig. 14 Behavior of nanofluid radial velocity for various δ

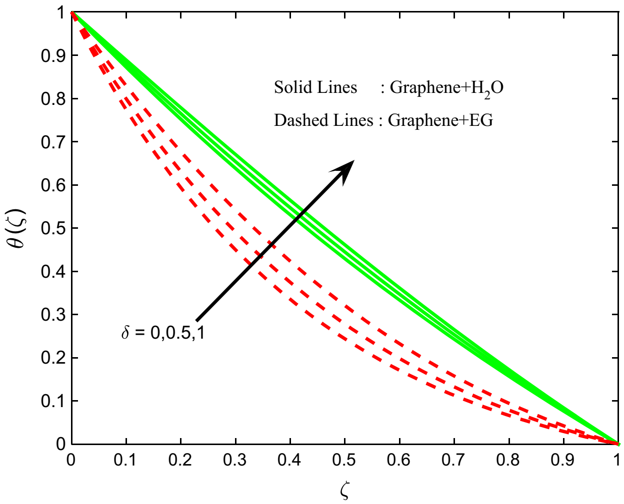

Fig. 15 Behavior of nanofluid temperature for various δ

improves. Physically, higher Re ensures decay in the viscous nature of the fluid and thus less resistance is required for the fluid motion. Graphene + water based nanofluid shows higher boundary layer compared with Graphene + Ethylene glycol-based nanofluid. This nature may be because viscosity of water is less compared with ethylene glycol. Figures 6 and 7 portray the authority of radiation parameter (R) on axial $f(\zeta)$ velocity and temperature $\theta(\zeta)$ profile. It is pragmatic that increment in R improves the $f(\zeta)$ velocity and reduces the $\theta(\zeta)$ profile in both Graphene + Ethylene glycol and Graphene + water nanofluid. It may be due to rotation of the disk. It is also evident that Graphene + water based nanofluid shows higher temperature distribution compared to Graphene + Ethylene glycol based nanofluid. Figures 8–10 illustrate the influence of larger values of Hartman number (M) on $f(\zeta), f'(\zeta), g(\zeta)$ velocity profiles. Existence of the Lorentz force decreases tangential and radial velocity distributions. Because of the rotation, larger value of M has no greater influence on axial velocity and thus velocity increases in this direction. Magnitude of velocity distribution is higher for Graphene + water based nanofluid in case of axial direction, whereas in tangential and radial direction magnitude of velocity distribution is higher for Graphene + Ethylene glycol based nanofluid. Figures 11 and 12 depict the influence of increasing values of nonlinear convection variable due to temperature $\left(\beta_t\right)$ on $f(\zeta)$ and $f'(\zeta)$ profiles. Improvement in β_t increases $f'(\zeta)$ profiles and decreases $f(\zeta)$ profiles. In $f(\zeta)$ case Graphene + water profiles shows higher distribution in velocity, whereas in $f'(\zeta)$ case Graphene + Ethylene glycol mixture shows higher distribution in velocity. In Figs. 13–15, the results due to the improvement in heat generation variable (δ) can be observed. Improvement in δ lessens $f(\zeta)$ velocity profiles and improves $f'(\zeta)$ and $\theta(\zeta)$ profiles. Graphene + water nanofluid shows higher velocity distribution in case of $f(\zeta)$ similar to temperature distribution $\theta(\zeta)$ profiles. However, Graphene + Ethylene glycol based nanofluid depicts higher distribution in velocity in case of $f'(\zeta)$.

The coefficient of skin friction (radial and tangential direction, $\left(c_f(\mathrm{Re})^{\frac{1}{2}}, c_g(\mathrm{Re})^{\frac{1}{2}}\right)$) and Nusselt number $\left(-Nu(\mathrm{Re})^{-\frac{1}{2}}\right)$ for Graphene + H_2O and Graphene + EG nanofluid are portrayed in Tables 2 and 3. It is observed that improvement in Reynolds number (Re) improves $c_f(\mathrm{Re})^{\frac{1}{2}}$ and the $-Nu(\mathrm{Re})^{\frac{(-1)}{2}}$ but decreases $c_g(\mathrm{Re})^{\frac{1}{2}}$ for both nanofluid Graphene + water and Graphene + Ethylene glycol. Increasing radiation parameter (R) diminishes $c_f(\mathrm{Re})^{\frac{1}{2}}$ and elevates $c_g(\mathrm{Re})^{\frac{1}{2}}$ and $-Nu(\mathrm{Re})^{\frac{(-1)}{2}}$ in both the nanofluid Graphene + water and Graphene + Ethylene glycol. Improvement in Hartman number (M) decreases $c_f(\mathrm{Re})^{\frac{1}{2}}$ and $c_g(\mathrm{Re})^{\frac{1}{2}}$ and the $-Nu(\mathrm{Re})^{\frac{(-1)}{2}}$ in case of Graphene + water and Graphene + Ethylene glycol nanofluid. Improvement in nonlinear convection variable due to temperature $\left(\beta_t\right)$ and heat generation variable (δ) elevates $c_f(\mathrm{Re})^{\frac{1}{2}}$ and $-Nu(\mathrm{Re})^{\frac{(-1)}{2}}$ but decreases $c_g(\mathrm{Re})^{\frac{1}{2}}$ in both the nanofluid Graphene + water and Graphene + Ethylene glycol. Ethylene glycol-based graphene nanofluid takes less time for execution as compared to water based nanofluid.

Conclusions

Flow and heat transfer of graphene nanoparticles in water- and ethylene glycol based nonlinear convective flow between porous rotating disk and fixed impermeable are studied. The main results are as follows:

- Intensification in Re ensures decrement in $f(\zeta), g(\zeta), \theta(\zeta)$ profiles, whereas $f'(\zeta)$ profile improves.
- Increment in R reduces the $\theta(\zeta)$ profile in graphene and water mixture and graphene and ethylene glycol mixture.
- Existence of Lorentz force decreases tangential and radial velocity distribution.
- Ethylene glycol based graphene nanoparticles take less time for execution compared to water base.
- Improvement in β_t increases $f'(\zeta)$ profiles and decreases $f(\zeta)$ profiles.
- Improvement in δ lessens $f(\zeta)$ velocity profiles and improves $f'(\zeta)$ and $\theta(\zeta)$ profiles.
- Improvement in M decreases skin friction $\left(c_f(\mathrm{Re})^{\frac{1}{2}}, c_g(\mathrm{Re})^{\frac{1}{2}}\right)$ along with $-Nu(\mathrm{Re})^{\frac{(-1)}{2}}$ in both the nanofluid graphene and ethylene glycol and graphene and water.
- Improvement in β_t and δ elevates $c_f(\mathrm{Re})^{\frac{1}{2}}$ and Nusselt number but decreases $c_g(\mathrm{Re})^{\frac{1}{2}}$ in both the nanofluid graphene and water and graphene and ethylene glycol.

References

1. Wu W, Xiao B, Hu J, Yuan S, Hu C. Experimental investigation on the air-liquid two-phase flow inside a grooved rotating-disk system: flow pattern maps. Appl Therm Eng. 2018;133:33–8. https://doi.org/10.1016/j.applthermaleng.2018.01.031.
2. Rizwan UH, Noor NFM, Khan ZH. Numerical simulation of water based magnetite nanoparticles between two parallel disks. Adv Powder Technol. 2016. https://doi.org/10.1016/j.apt.2016.05.020.
3. Turkyilmazoglu M. Fluid flow and heat transfer over a rotating and vertically moving disk. Phys Fluids. 2018. https://doi.org/10.1063/1.5037460.
4. Turkyilmazoglu M. Flow and heat simultaneously induced by two stretchable rotating disks. Phys Fluids. 2016. https://doi.org/10.1063/1.4945651.
5. Turkyilmazoglu M. Purely analytic solutions of magnetohydrodynamic swirling boundary layer flow over a porous rotating disk. Comput Fluids. 2010;39:793–9. https://doi.org/10.1016/j.compfluid.2009.12.007.
6. Rashidi MM, Abelman S, Mehr NF. Entropy generation in steady MHD flow due to a rotating porous disk in a nanofluid. Int J Heat Mass Transf. 2013;62:515–25. https://doi.org/10.1016/j.ijheatmasstransfer.2013.03.004.
7. Rashidi MM, Pour SAM, Hayat T, Obaidat S. Analytic approximate solutions for steady flow over a rotating disk in porous medium with heat transfer by homotopy analysis method. Comput Fluids. 2012;54:1–9. https://doi.org/10.1016/j.compfluid.2011.08.001.
8. Qayyum S, Ijaz M, Hayat T, Alsaedi A. Comparative investigation of five nanoparticles in flow of viscous fluid with Joule heating and slip due to rotating disk. Phys B. 2018;534:173–83. https://doi.org/10.1016/j.physb.2018.01.044.
9. Pourmehran O, Sarafraz MM, Rahimi-gorji M, Ganji DD. Rheological behaviour of various metal-based nano-fluids between rotating discs. J Taiwan Inst Chem Eng. 2018. https://doi.org/10.1016/j.jtice.2018.04.004.
10. Attia HA. Steady flow over a rotating disk in porous medium with heat transfer. Nonlinear Anal Model Control. 2009;14:21–6.
11. Mellor GL, Chapple PJ, Stokes VK. On the flow between a rotating and a stationary disk. J Fluid Mech. 1968;31:95–112. https://doi.org/10.1017/S0022112068000054.
12. Kavenuke DP, Massawe E, Makinde OD. Modeling laminar flow between a fixed impermeable disk and a porous rotating disk. Afr J Math Comput Sci Res. 2009;2:157–62.
13. Awati VB, Makinde OD, Jyoti M. Computer-extended series solution for laminar flow between a fixed impermeable disk and a porous rotating disk. Eng Comput. 2018;35:1655–74. https://doi.org/10.1108/EC-01-2017-0021.
14. Choi SUS, Eastman JA. Enhancing thermal conductivity of fluids with nanoparticles. ASME Pub Fed. 1995;231:99–106.
15. Sarafraz MM, Hormozi F, Kamalgharibi M. Sedimentation and convective boiling heat transfer of CuO-water/ethylene glycol nanofluids. Heat Mass Transf. 2014;50(9):1237–49.
16. Salari E, Peyghambarzadeh SM, Sarafraz MM, Hormozi F, Nikkhah V. Thermal behavior of aqueous iron oxide nano-fluid as a coolant on a flat disc heater under the pool boiling condition. Heat Mass Transf. 2017;53(1):265–75.
17. Kamalgharibi M, Hormozi F, Zamzamian SAH, Sarafraz MM. Experimental studies on the stability of CuO nanoparticles dispersed in different base fluids: influence of stirring, sonication and surface active agents. Heat Mass Transf. 2016;52(1):55–62.
18. Sajid MU, Ali HM. Thermal conductivity of hybrid nanofluids: a critical review. Int J Heat Mass Transf. 2018;126:211–34.
19. Imtiaz M, Hayat T, Alsaedi A, Ahmad B. Convective flow of carbon nanotubes between rotating stretchable disks with thermal radiation effects. Int J Heat Mass Transf. 2016;101:948–57. https://doi.org/10.1016/j.ijheatmasstransfer.2016.05.114.
20. Salari E, Peyghambarzadeh SM, Sarafraz MM, Hormozi F. Boiling thermal performance of TiO_2 aqueous nanofluids as a coolant on a disc copper block. Period Polytech Chem Eng. 2016;60(2):106–22.
21. Hayat T, Rashid M, Ijaz M, Alsaedi A. Melting heat transfer and induced magnetic field effects on flow of water based nano fluid over a rotating disk with variable thickness. Results Phys. 2018;9:1618–30. https://doi.org/10.1016/j.rinp.2018.04.054.
22. Bachok N, Ishak A, Pop I. Flow and heat transfer over a rotating porous disk in a nanofluid. Phys B. 2011;406:1767–72. https://doi.org/10.1016/j.physb.2011.02.024.
23. Ellahi R, Zeeshan A, Hussain F, Safaei MR. Simulation of cavitation of spherically shaped hydrogen bubbles through a tube nozzle with stenosis. Int J Numer Meth Heat Fluid Flow. 2020. https://doi.org/10.1108/HFF-04-2019-0311.
24. Ellahi R, Hussain F, Abbas SA, Sarafraz MM, Goodarzi M, Shadloo MS. Study of two-phase Newtonian nanofluid flow hybrid with Hafnium particles under the effects of slip. Inventions. 2020;5:6.
25. Nazari S, Ellahi R, Sarafraz MM, Safaei MR, Asgari A, Akbari OA. Numerical study on mixed convection of a non-Newtonian nanofluid with porous media in a two lid-driven square cavity. J Therm Anal Calorim. 2019;140:1121–45.
26. Maleki H, Alsarraf J, Moghanizadeh A, Hajabdollahi H, Safaei MR. Heat transfer and nanofluid flow over a porous plate with radiation and slip boundary Zonditions. J Cent South Univ. 2019;26(5):1099–115.
27. Maleki H, Safaei MR, Alrashed AA, Kasaeian A. Flow and heat transfer in non-Newtonian nanofluids over porous surfaces. J Therm Anal Calorim. 2019;135(3):1655–66.
28. Giwa SO, Sharifpur M, Goodarzi M, Alsulami H, Meyer JP. Influence of base fluid, temperature, and concentration on the thermophysical properties of hybrid nanofluids of alumina–ferrofluid: experimental data, modeling through enhanced ANN, ANFIS, and curve fitting. J Therm Anal Calorim. 2020. https://doi.org/10.1007/s10973-020-09372-w.
29. Peng Y, Zahedidastjerdi A, Abdollahi A, Amindoust A, Bahrami M, Karimipour A, Goodarzi M. Investigation of energy performance in a U-shaped evacuated solar tube collector using oxide added nanoparticles through the emitter, absorber and transmittal environments via discrete ordinates radiation method. J Therm Anal Calorim. 2020;139:2623–31.
30. Ahmadi MH, Mohseni-Gharyehsafa B, Ghazvini M, Goodarzi M, Jilte RD, Kumar R. Comparing various machine learning approaches in modeling the dynamic viscosity of CuO/water nanofluid. J Therm Anal Calorim. 2019;139(4):2585–99.
31. Yousefzadeh S, Rajabi H, Ghajari N, Sarafraz MM, Akbari OA, Goodarzi M. Numerical investigation of mixed convection heat transfer behavior of nanofluid in a cavity with different heat transfer areas. J Therm Anal Calorim. 2019;77:195–205.
32. Arasteh H, Mashayekhi R, Goodarzi M, Motaharpour SH, Dahari M, Toghraie D. Heat and fluid flow analysis of metal foam embedded in a double-layered sinusoidal heat sink under local thermal non-equilibrium condition using nanofluid. J Therm Anal Calorim. 2019;138(2):1461–76.
33. Sarafraz MM, Tlili I, Tian Z, Khan AR, Safaei MR. Thermal analysis and thermo-hydraulic characteristics of zirconia–water nanofluid under a convective boiling regime. J Therm Anal Calorim. 2019;139(4):2413–22.
34. Maleki H, Safaei MR, Togun H, Dahari M. Heat transfer and fluid flow of pseudo-plastic nanofluid over a moving permeable plate with viscous dissipation and heat absorption/generation. J Therm Anal Calorim. 2019;135(3):1643–54.

35. Sajid MU, Ali HM. Recent advances in application of nanofluids in heat transfer devices: a critical review. Renew Sustain Energy Rev. 2019;103:556–92.
36. Sajid MU, Ali HM, Sufyan A, Rashid D, Zahid SU, Rehman WU. Experimental investigation of TiO_2–water nanofluid flow and heat transfer inside wavy mini-channel heat sinks. J Therm Anal Calorim. 2019;137(4):1279–94.
37. Ali HM, Babar H, Shah TR, Sajid MU, Qasim MA, Javed S. Preparation techniques of TiO_2 nanofluids and challenges: a review. Appl Sci. 2018;8(4):587.
38. Wahab A, Hassan A, Qasim MA, Ali HM, Babar H, Sajid MU. Solar energy systems—potential of nanofluids. J Mol Liq. 2019;289:111049.
39. Szilágyi IM, Santala E, Heikkilä M, Kemell M, Nikitin T, Khriachtchev L, Leskelä M. Thermal study on electrospun polyvinylpyrrolidone/ammonium metatungstate nanofibers: optimising the annealing conditions for obtaining WO_3 nanofibers. J Therm Anal Calorim. 2011;105(1):73.
40. Jaćimović Ž, Kosović M, Kastratović V, Holló BB, Szécsényi KM, Szilágyi IM, Rodić M. Synthesis and characterization of copper, nickel, cobalt, zinc complexes with 4-nitro-3-pyrazolecarboxylic acid ligand. J Therm Anal Calorim. 2018;133(1):813–21.
41. Justh N, Berke B, László K, Szilágyi IM. Thermal analysis of the improved Hummers, synthesis of graphene oxide. J Therm Anal Calorim. 2018;131(3):2267–72.
42. Holló BB, Ristić I, Budinski-Simendić J, Cakić S, Szilágyi IM, Szécsényi KM. Synthesis, spectroscopic and thermal characterization of new metal-containing isocyanate-based polymers. J Therm Anal Calorim. 2018;132(1):215–24.
43. Gangadevi R, Vinayagam BK. Experimental determination of thermal conductivity and viscosity of different nanofluids and its effect on a hybrid solar collector. J Therm Anal Calorim. 2019;136(1):199–209.
44. Jeyaseelan TR, Azhagesan N, Pethurajan V. Thermal characterization of $NaNO_3/KNO_3$ with different concentrations of Al_2 O_3 and TiO_2 nanoparticles. J Therm Anal Calorim. 2019;136(1):235–42.
45. Sarafraz MM, Safaei MR. Diurnal thermal evaluation of an evacuated tube solar collector (ETSC) charged with graphene nanoplatelets-methanol nano-suspension. Renew Energy. 2019;142:364–72.
46. Sarafraz MM, Safaei MR, Tian Z, Goodarzi M, Bandarra Filho EP, Arjomandi M. Thermal assessment of nano-particulate graphene-water/ethylene glycol (WEG 60: 40) nano-suspension in a compact heat exchanger. Energies. 2019;12(10):1929.
47. Sarafraz MM, Tlili I, Tian Z, Bakouri M, Safaei MR, Goodarzi M. Thermal evaluation of graphene nanoplatelets nanofluid in a fast-responding HP with the potential use in solar systems in smart cities. Appl Sci. 2019;9(10):2101.
48. Sarafraz MM, Yang B, Pourmehran O, Arjomandi M, Ghomashchi R. Fluid and heat transfer characteristics of aqueous graphene nanoplatelet (GNP) nanofluid in a microchannel. Int Commun Heat Mass Transfer. 2019;107:24–33.
49. Raju CSK, Saleem S, Al-Qarni MM, Upadhya SM. Unsteady nonlinear convection on Eyring–Powell radiated flow with suspended graphene and dust particles. Microsyst Technol. 2019;25(4):1321–31.
50. Mamatha Upadhya S, Mahesha A, Raju CSK, Shehzad SA, Abbasi FM. Flow of Eyring-Powell dusty fluid in a deferment of aluminum and ferrous oxide nanoparticles with Cattaneo-Christov heat flux. Powder Technol. 2018;340:68–766.
51. Mamatha SU, Raju CSK, Putta Durga P, Ajmath KA, Oluwole Daniel M. Exponentially decaying heat source on MHD tangent hyperbolic two-phase flows over a flat surface with convective conditions. Defect Diff Forum. 2018;387:286–95.
52. Upadhya SM, Raju CSK, Saleem S, Alderremy AA. Modified Fourier heat flux on MHD flow over stretched cylinder filled with dust, Graphene and silver nanoparticles. Results Phys. 2018;9:1377–85. https://doi.org/10.1016/j.rinp.2018.04.038.
53. Mamatha Upadhya S, Raju CSK. Unsteady flow of Carreau fluid in a suspension of dust and graphene nanoparticles with Cattaneo–Christov heat flux. J Heat Transf. 2018;140(9):092401.
54. Sharma RP, Makinde OD, Animasaun IL. Buoyancy effects on MHD unsteady convection of a radiating chemically reacting fluid past a moving porous vertical plate in a binary mixture. Defect Diff Forum. 2018;387:308–18.
55. Santhosh HB, Raju CSK. Unsteady Carreau radiated flow in a deformation of graphene nanoparticles with heat generation and convective conditions. J Nanofluids. 2018;7(6):1130–7.
56. Nayak MK, Shaw S, Makinde OD, Chamkha AJ. Investigation of partial slip and viscous dissipation effects on the radiative tangent hyperbolic nanofluid flow past a vertical permeable riga plate with internal heating: Bungiorno model. J Nanofluids. 2019;8(1):51–62.
57. Eid MR, Makinde OD. Solar radiation effect on a magneto nanofluid flow in a porous medium with chemically reactive species. Int J Chem React Eng. 2018. https://doi.org/10.1515/ijcre-2017-0212.
58. Stewartson K. On the flow between two rotating coaxial disks. Proc Comb Phil Soc. 1953;49:333–41.

Publisher's Note Springer Nature remains neutral with regard to jurisdictional claims in published maps and institutional affiliations.